


Article

Obsidian as a Raw Material for Eco-Friendly Synthesis of Magnetic Zeolites

Claudia Belviso ^{1,*}, Davide Peddis ^{2,3}, Gaspare Varvaro ⁴, Maryam Abdolrahimi ^{3,4}, Andrea Pietro Reverberi ² and Francesco Cavalcante ¹

¹ Istituto di Metodologie per l'Analisi Ambientale—CNR, 85050 Tito Scalo, Italy; francesco.cavalcante@imaa.cnr.it

² Departments of Chemistry and Industrial Chemistry (DCIC), Università of Genova, 16146 Genova, Italy; davide.peddis@unige.it (D.P.); andrea.reverberi@unige.it (A.P.R.)

³ Istituto di Struttura della Materia—CNR, 00015 Monterotondo Scalo, Italy; abdolrahimi.ps66@yahoo.com

⁴ Dipartimento di Scienze, Università degli Studi Roma Tre, 00146 Roma, Italy; gaspare.varvaro@ism.cnr.it

* Correspondence: claudia.belviso@imaa.cnr.it; Tel.: +39-097-427-224

Received: 11 September 2020; Accepted: 15 October 2020; Published: 16 October 2020



Abstract: A sample of rhyolitic obsidian (OS) was used as raw material for zeolite synthesis by long (4 days) and fast (2 h)-aging hydrothermal processes. Zeolite synthesis was also performed by a fast (2 h) sonication method. The products were analysed by X-ray diffraction (XRD) and scanning electron microscopy (SEM) both immediately after and 3 years after their formation in order to determine the stability of synthetic materials according to the method used. The results confirm zeolitization of obsidian both by long-aging conventional hydrothermal heating and fast hydrothermal process. However, the data highlight the efficiency of direct ultrasound energy in achieving more stable zeolite crystals over time. These results carried out using a natural source, follow those already obtained using wastes and pure sources as raw materials thus providing a definitive validation of the different mechanisms controlling zeolite formation according to the process used. Moreover, the results confirm the effectiveness of ultrasonic energy in the formation of zeolites that are more stable over time. Due to the chemical composition of the obsidian precursor, all synthetic zeolites show good magnetic properties (i.e., saturation magnetization), in view to potential magnetic separation.

Keywords: obsidian; ultrasonic and hydrothermal water bath; zeolite; magnetic properties

1. Introduction

Zeolites are hydrated aluminosilicate minerals consisting of TO_4 tetrahedra ($T = \text{Si}$ or Al) which are connected by sharing corner oxygen atoms. They are characterized by peculiar and well-known properties (i.e., high surface area, porosity, and cation exchange capacity) making these minerals very useful in many applications [1–9]. However, with the aim to improve the zeolite use in some specific contexts (e.g., water pollution remediation), recent studies have been focused on the development of magnetic zeolites. Literature data have documented different methods to form magnetic zeolites, mainly based on addition of preformed iron oxide nanoparticles during the synthesis [10–13]. As an alternative we recently demonstrated that many kinds of magnetic zeolites can be obtained exploiting chemical composition of the precursors without the addition of external magnetic nanoparticles [14,15].

Due to the general growing demand for these materials, significant research activities have been devoted to zeolite synthesis also considering the economical stand, the environmental and safety implications for sustainable production [16]. As result, literature data have shown zeolite formation by different methods [17–28], mainly using processes at low aging temperatures [29–34]. In our previous manuscripts [35,36], the zeolite formation by conventional hydrothermal process or ultrasonic was

analysed. The experiments were performed using two different raw materials based on silica and aluminum. In both cases, the results indicated that the hydrothermal process is responsible for slower geopolymer transformation into well-defined zeolite crystals, whereas the fast precipitation mechanism determines the formation of metastable zeolites by sonication. The data showed that the two different approaches also control the stability of the synthetic products over the years [35,36].

Beside the processes, the use of different precursors has also been extensively explored. Zeolites have been formed from wastes [37–46], natural sources such as clay minerals [47–54] or by adding zeolite seeds in starting gel with or without organic templates [55–58]. Recently, natural cost-effective and green silica precursors such as diatomite and obsidian were also used [59–66]. Both materials are interesting natural precursors due to their relatively low cost and highly reactivity although the formation of zeolite type strongly depends on the elemental composition of these natural sources as well as on the used process. Kawano and Tomita [65] demonstrated that phillipsite and merlinoite formed from alteration of obsidian in NaOH and KOH solution, respectively whereas Mamedova [64] formed natrolite with high degree of crystallization by a hydrothermal method at 200 °C using a mixture of natural halloysite and obsidian. In our previous paper [62], small crystals of EMT-type zeolite were synthesized from an obsidian precursor. The data displayed that zeolite formed at a lower incubation temperature using seawater comparing to distilled water. However, with seawater, EMT showed higher metastable behavior as indicated by its competitive growth with P-type zeolite [62].

In the present study, the efficiency of ultrasonic versus hydrothermal water bath method to convert obsidian into zeolite was investigated. Moreover, the stability over the time of the synthetic products formed from this natural precursor will be studied. Finally, due to the potential complex magnetic and microstructural properties of the obsidian [67], magnetic characterization of the precursor and final products were performed.

2. Materials and Methods

A sample of rhyolitic obsidian (OS) collected at Punta delle Rocche Rosse (Lipari, Aeolian Islands, Italy), was used as raw material. It was pre-fused at 600 °C for 1 h with NaOH (1:1.2 weight ratio) and stirred for a night in a seawater solution. In detail, 8 g of pre-fused OS powder was mixed with 42 mL of seawater. Finally, the sample was submitted to three different aging processes in separate experiments: (i) a conventional hydrothermal process at 60 °C for 4 days (HY4d) [29,30]; (ii) a hydrothermal water bath method for 2 h at 60 °C (HY2h) [35,36]; (iii) an ultrasonic water bath process (240 W, 35 kHz) for 2 h at 60 °C (US2h) [35,36]. After all the aging processes, the solids and solutions were separated by centrifugation. The solids of all the samples were washed with the same amount of distilled water and dried in an oven at 80 °C. The mineralogical characterization of both OS and synthetic products (HY4d, HY2h US2h) were carried out by X-ray powder diffraction (XRD) using a Rint Miniflex powder diffractometer (Rigaku) with Cu-K α radiation. Morphological observations were performed by scanning electron microscopy (SEM, Supra 40, Zeiss,) equipped with an energy dispersive spectrometer (EDS). Chemical composition of obsidian was determined for its major elements by X-ray fluorescence (XRF, PW 1480, Philips).

DC magnetization measurements were investigated using MPMS XL-5 ($H_{\max} \pm 5T$, Quantum Design) and VSM ($H_{\max} \pm 2T$, Microsense) magnetometers. Each sample, in the form of powder dispersed within epoxy resin, is placed inside the capsules of polycarbonate. The epoxy resin is used to avoid any powder movement during the measurements.

3. Results

3.1. Raw Materials

Figure 1 shows the XRD pattern and SEM images of the obsidian raw material. The X-ray profile shows the typical broad band of a glass material (Figure 1a) confirmed by the irregular particle morphology displayed by the scanning electron micrographs in Figure 1b. The chemical data (Table 1)

indicate that obsidian is characterized by a high amount of SiO_2 (75.48%) and relative low percentage of Al_2O_3 (11.75%) with a following $\text{SiO}_2/\text{Al}_2\text{O}_3$ ratio of 6.42. The percentage of K_2O is 5.41%, whereas the amounts of Na_2O and Fe_2O_3 are 3.47% and 2.87%, respectively.

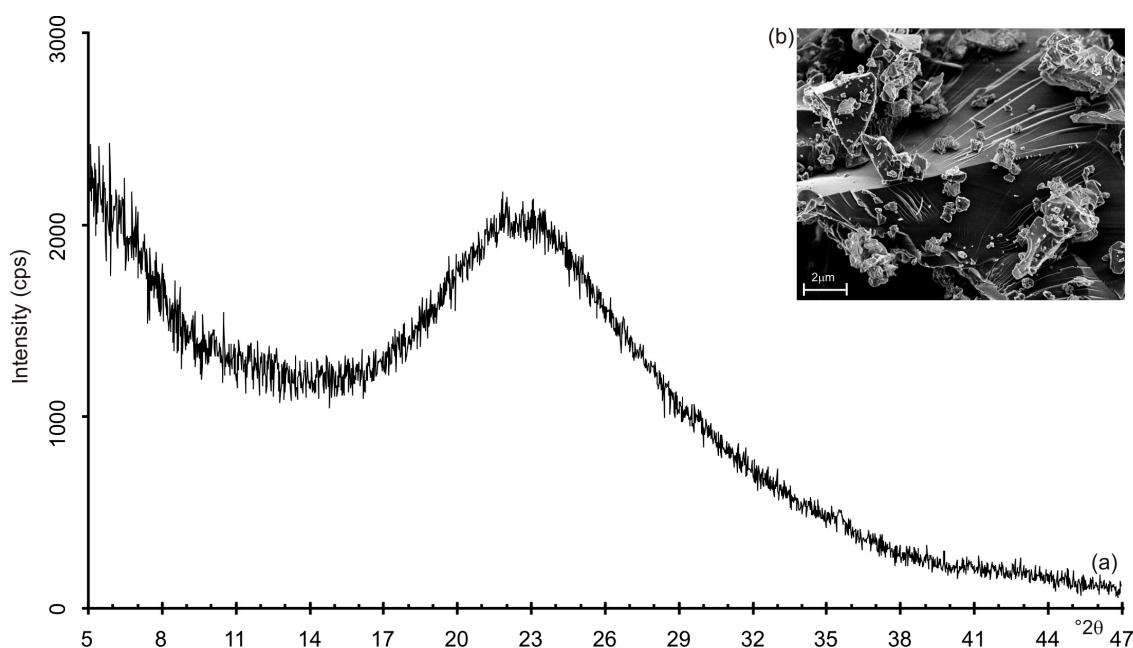


Figure 1. (a) X-ray pattern and (b) SEM picture of rhyolitic obsidian.

Table 1. Chemical composition of obsidian raw material.

Major Constituents (wt.%)											
Sample	Na_2O	MgO	Al_2O_3	SiO_2	P_2O_5	K_2O	CaO	TiO_2	MnO	Fe_2O_3	$\text{SiO}_2/\text{Al}_2\text{O}_3$
OS	3.47	0.00	11.75	75.48	0.02	5.41	0.81	0.11	0.10	2.87	6.42
Trace elements (ppm)											
Sample	Ni	Co	Sr	Zr	Cu	Zn	As	Rb	Sn	Cs	Pb
OS	9.75	2.25	17.00	191.00	4.67	60.01	33.00	312.00	30.00	23.00	27.00

Finally, Table 2 shows the chemical composition and salinity of the natural seawater sample used. The data indicate a composition comparable with the typical average values of seawater.

Table 2. Seawater composition (values in g/L; salinity g/kg).

Sample	Salinity	Si	Al	Cl	Na	Mg	Ca	K
Natural seawater	35.00	0.0015	0.0011	19.962	7.727	1.375	0.538	0.014

3.2. Starting Process of Obsidian Zeolitization

Figure 2 shows X-ray diffraction data after both HY and US processes. The XRD pattern of HY4d (Figure 2a) indicates the dominant presence of EMT-type zeolite whose typical hexagonal plate shape is shown by the SEM pictures in Figure 3. However, it cannot be excluded the presence of low amount of a faujasite type zeolite (FAU) phase and geopolymers as indicated by the broad band from 20 to 37° 2θ on the X-ray profile. XRD pattern of the obsidian sample incubated by the hydrothermal water bath method for 2 h (Figure 2b) indicates the presence of low amount of EMT-type zeolite confirming the presence of geopolymeric materials. Low percentages of sodalite and halite are also detectable. The presence of EMT-type zeolite is more evident in US2h XRD profile after ultrasonic water bath process for 2 h (Figure 2c). In this sample the amount of halite is quite high.

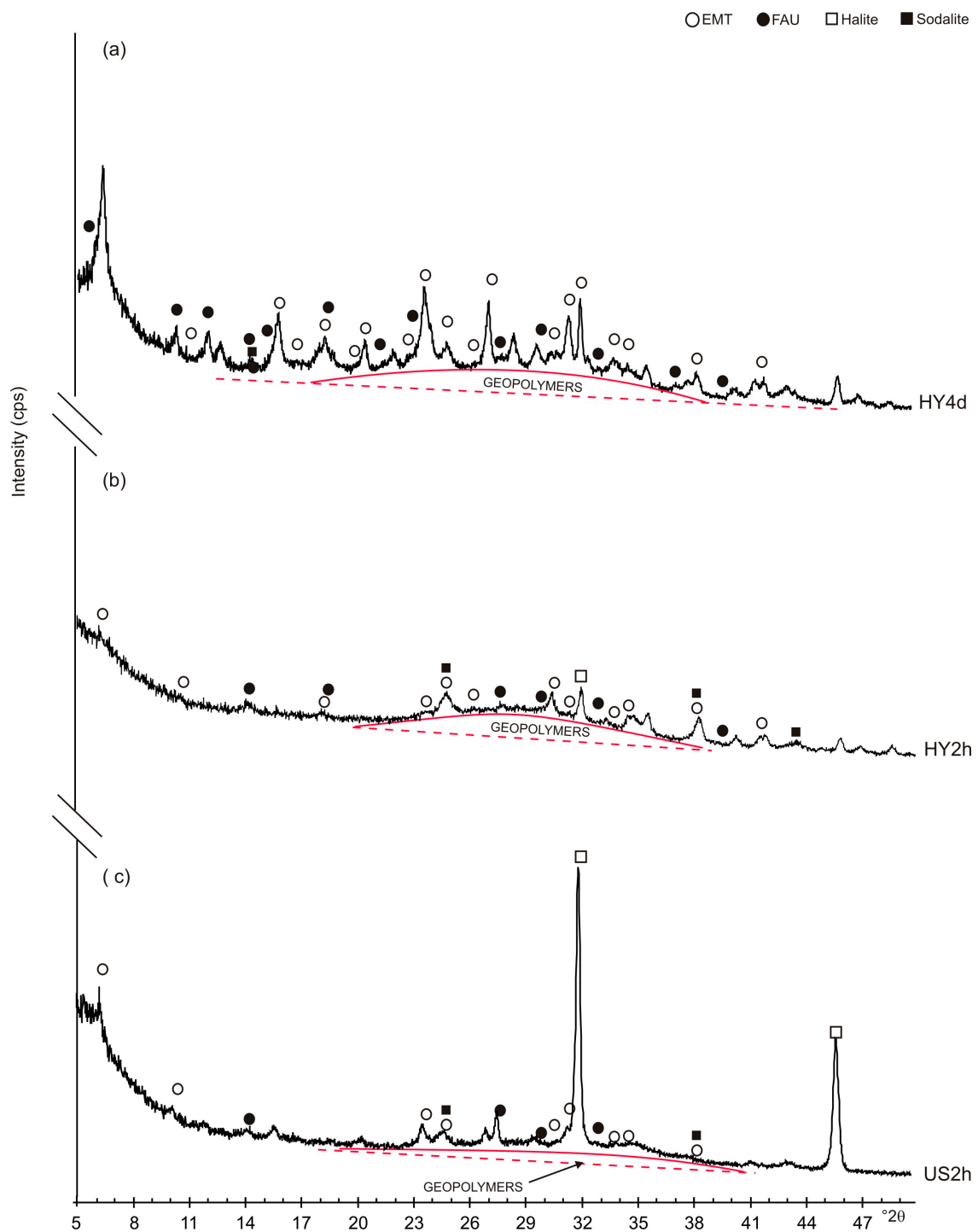


Figure 2. XRD patterns of the sample after: (a) conventional hydrothermal process at 60 °C for 4 days (HY4d); (b) hydrothermal water bath method for 2 h at 60 °C (HY2h) and (c) ultrasonic water bath (240 W; 35 kHz) for 2 h at 60 °C (US2h).

The field dependence of the magnetization of the OS raw material and all the synthetic zeolite samples has been investigated at 300 K (Figure 4a). The OS sample shows a ferromagnetic-like behavior with a very low saturation magnetization ($M_s \cong 0.96 \text{ A m}^2 \text{ kg}^{-1}$), in agreement with the values found by other authors for obsidian samples [67].

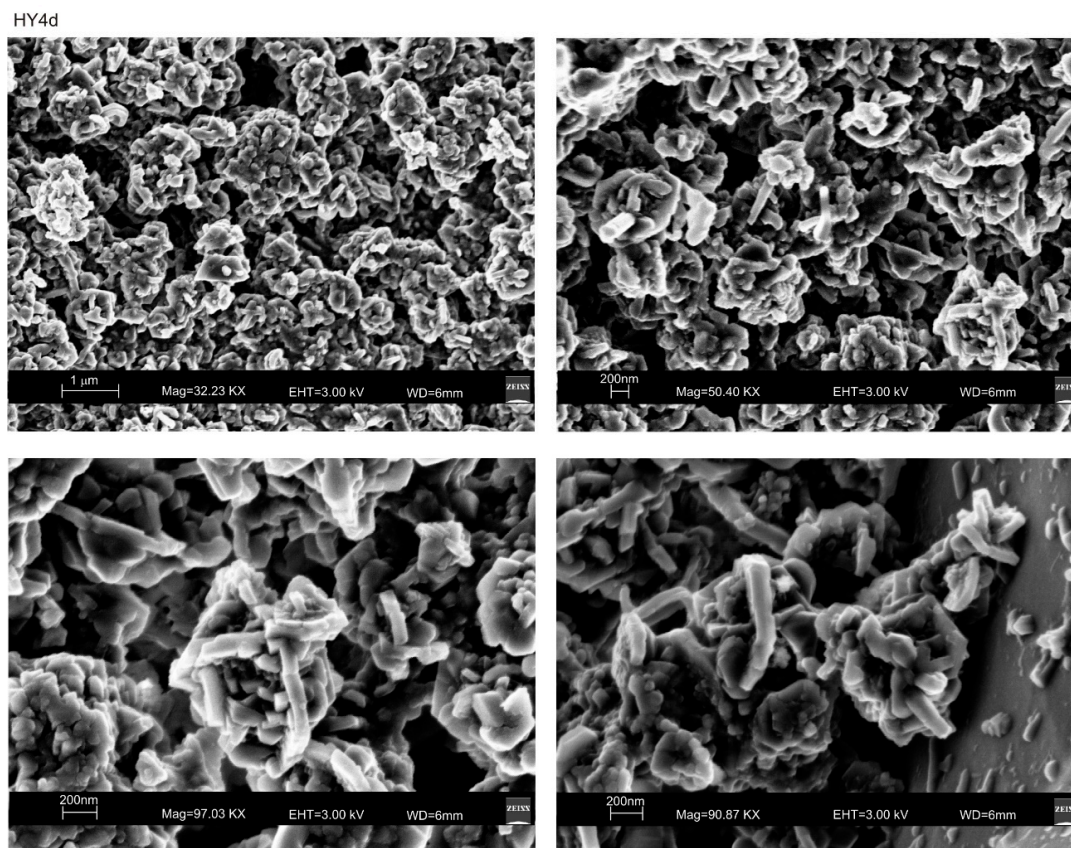


Figure 3. SEM images of EMT-type zeolite formed by 4-days conventional hydrothermal process (HY4d).

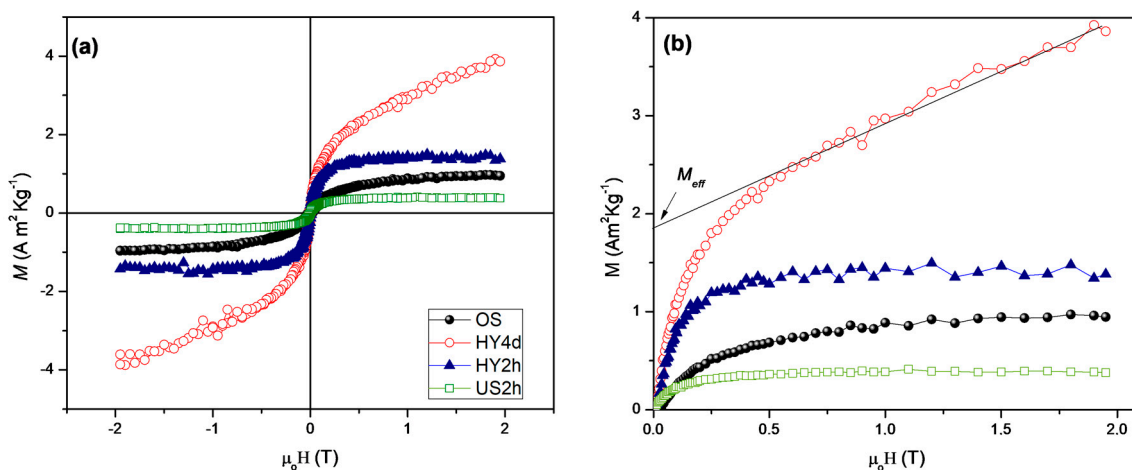


Figure 4. (a) Field dependence of magnetization recorded at 300 K; (b) Magnification M vs. H in the range 0–2 T. For all samples, extrapolation to zero of the high field linear portion of the magnetisation was used to determine the effective magnetic moment (M_{eff}).

This indicates that the magnetic behavior is dominated by some ferrimagnetic oxides like maghemite ($\gamma\text{-Fe}_2\text{O}_3$) or magnetite (Fe_3O_4) present in quite low percentages, in agreement with the chemical analysis. Both HY2d and US2h show also ferromagnetic-like behavior with M_s values of ~ 1.32 and $\sim 0.43 \text{ A m}^2 \text{ kg}^{-1}$ respectively. HY2d shows an increase of 27% of M_s with respect to the OS raw material, indicating that the hydrothermal treatment promotes the formation and stabilization of ferro(ferrimagnetic) oxides. On the other hand, ultrasound treatment (US2h sample) brings about a strong reduction ($\sim 56\%$) of M_s with respect to OS sample, inducing us to believe that a higher

fraction of antiferromagnetic oxides (e.g., hematite, α Fe₂O₃) and hydroxides (e.g., goethite, FeOOH) is present [68].

This landscape drastically changes in the samples HY4d, showing an antiferromagnetic behavior superimposed to a small ferromagnetic contribution in the lower field region [15]. To quantify the effective magnetic moment (M_{eff}) due to the ferro(ferri)magnetic component, the extrapolation to zero of the high-field linear portion can be used (Figure 4b) [15]. M_{eff} value is around 1.85 A m² kg⁻¹, that is much higher what is expected for nanostructured hematite (<0.5 A m² kg⁻¹) indicating that the ferromagnetic contribution could be ascribed to the presence of ferro (ferri)magnetic oxides and not to uncompensated spin of nanostructured hematite.

3.3. Synthetic Products over the Time

In order to determine the stability of the synthetic products over the time, all the synthetic products were analysed again by XRD and SEM three years after their formation. Figure 5 shows XRD pattern of HY4d_3y, HY2d_3y and US2h_3y. The data indicate that the zeolites formed after 4 days of a conventional hydrothermal process and by the ultrasonic water bath process for 2 h are characterized by relatively stable behavior. In detail, XRD pattern of HY4d_3y (Figure 5a) indicates the presence of EMT-type zeolite combined with a lower amount of FAU. However, the peaks of sodalite seem to be higher comparing to the starting products (HY4d) (Figure 2a). The sample formed by a fast ultrasonic treatment (US2h_3y, Figure 5c) also shows a quite stable behavior three years after the zeolite formation (see Figure 2c), whereas a clear phase transformation takes place over the three years in the zeolite formed by the fast hydrothermal water bath method (HY2h). The X-ray profile in Figure 5b, in fact, displays the presence of sodalite as the main crystalline phase whereas the prepared sample is characterized by the presence of large amount of geopolymers and by low percentages of both EMT and FAU, together with low sodalite (Figure 2b).

4. Discussion

The results of this study can be considered as conclusive data confirming the role of different processes in controlling both the mechanism of zeolite formation and the stability of synthetic products over the time, regardless of the raw material used.

Our previous data already demonstrated that obsidian can be successfully used as a precursor material for the organic-template-free EMT-type zeolite synthesis by a conventional hydrothermal process at 60 °C using a seawater solution [62]. Similarly, in other previous works we showed that different crystallization mechanisms control the zeolite synthesis according to the processes used for their formation [35,36]. In those papers, a waste material (fly ash) and Na₂O-Al₂O₃-SiO₂-H₂O precursor system were used to perform the experiments.

In the present study, we used one of the last types of natural raw material which remains to be investigated as a precursor to compare the efficiency of fast hydrothermal and ultrasonic water bath methods (2 h of treatment) in both type and zeolite stability over the time. Moreover, we also investigated the differences in both mechanism and zeolite stability between conventional long (4 days) and fast-aging hydrothermal processes (2 h).

The results indicate that all the synthetic products are characterized by the presence of EMT-type zeolite as dominant crystalline phase. However, HY4d and HY2h also show the presence of larger amount of geopolymers comparing to the US2h. The sonicated sample, instead, is characterized by higher amount of halite.

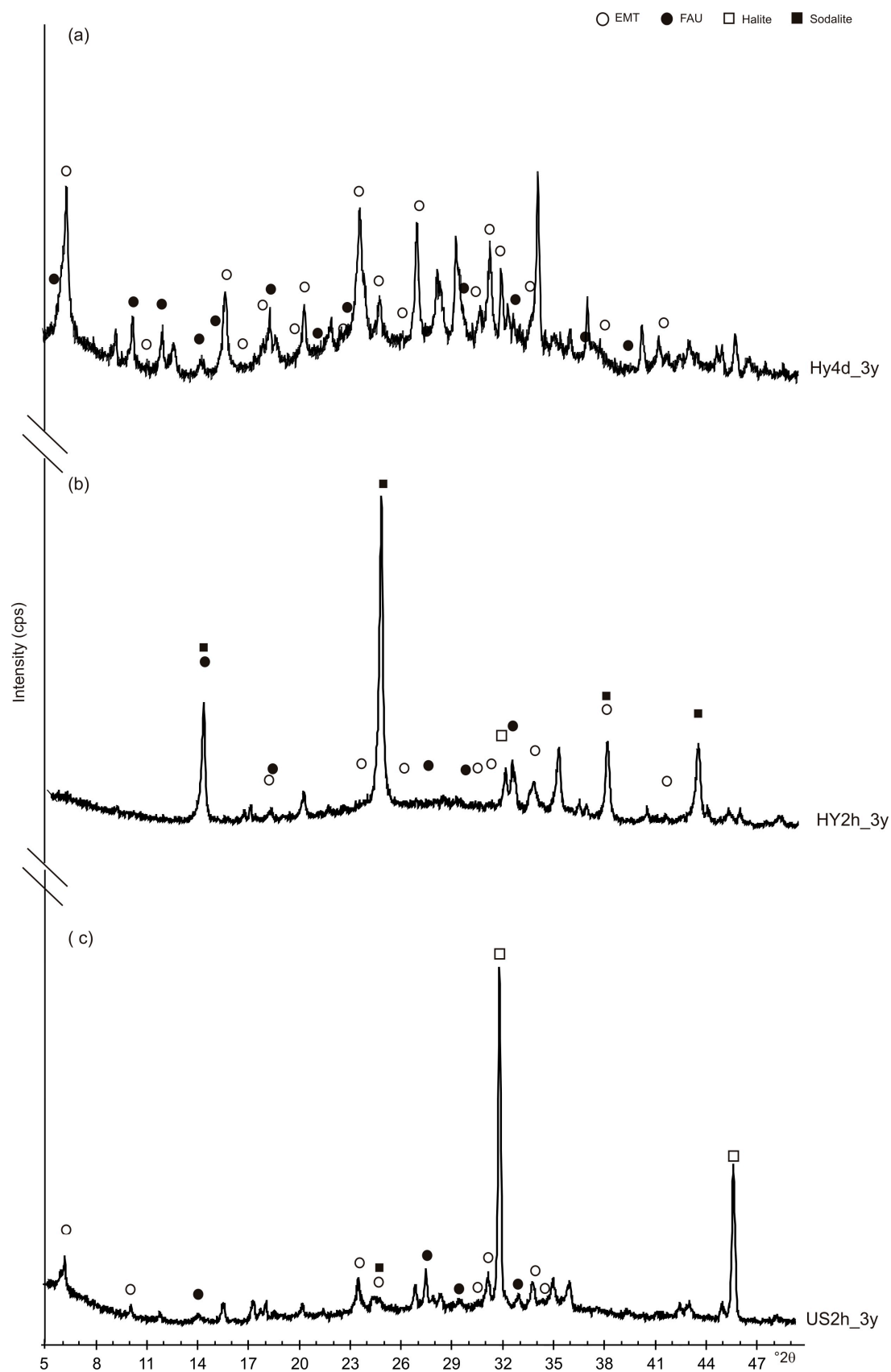


Figure 5. XRD profiles of the samples three years after their synthesis: (a) HY4d_3y; (b) HY2h_3y and (c) US2h_3y.

The differences between the investigated samples can be explained considering the crystallization mechanism related to the methods used. In our hypothesis EMT and FAU formation by hydrothermal process is controlled by a double-step mechanism characterized by geopolymer precipitation from saturated solution followed by a slow zeolite growth involving the amorphous mass. This hypothesis is in accordance with the results obtained using both waste sources [35] and pure reagents [36]. It also explains the presence of a larger amount of geopolymers in HY4d and HY2h as well as the behavior of these samples over time. The results, in fact, indicate that three years after their formation, HY2h_3y shows the presence of sodalite as its main phase (Figure 5b), thus confirming that the sample formed by fast hydrothermal water-bath method changed its mineralogical composition transforming the metastable EMT and FAU into a more stable form [69] through a progressive action involving the geopolymer phase.

However, the obsidian sample treated by a long-aging hydrothermal process does not show the same behavior. Three years after its formation, HY4d_3y, as opposed to HY2h_3y, is not characterized by the sole presence of sodalite. Its XRD pattern, in fact, shows a mineralogical composition qualitatively comparable with the starting one. This data suggests that the 4 days-aging hydrothermal process allows a more complete development of the double-step process for the zeolite formation, thus ensuring that the crystallization mechanism takes place slowly and therefore affording greater stability over time to the newly formed minerals. On the other hand, stopping this mechanism just two hours after activation (i.e., HY2h sample), determines the formation of EMT and FAU seeds with a stronger metastable behavior particularly displayed in a relative faster transformation at solid-state over time.

The presence of a high amount of halite and the stability over time of the samples formed by the fast ultrasonic water bath method indicate that the crystallization mechanism by sonication is controlled by a precipitation process, as already demonstrated in our previous papers [35,36]. The action of sonication improves both Na, Al, Si and Cl saturation and causes the disruption of nuclei already laid down in the medium, thus increasing the number of nuclei that quickly precipitate to form EMT and FAU-type zeolite together with halite.

Moreover, the magnetic results indicate that OS, HY2h and US2h show a ferromagnetic-like behavior while the fast hydrothermal and ultrasonic water bath treatment affect the saturation magnetization of the OS raw material. On the other hand, the long aging hydrothermal process dramatically changed the magnetic behavior, showing an antiferromagnetic-like behavior with a weak ferromagnetic contribution. The effective magnetic moment indicates that the ferromagnetic contribution could be due to the presence of ferro(ferri)magnetic oxides.

5. Concluding Remarks

The data indicate that obsidian can be converted into zeolitic material, mainly EMT-type zeolites exhibiting magnetic properties, by applying three different methods at low temperature (60 °C) and using a seawater solution. The synthesis was performed using fast hydrothermal or ultrasonic water bath methods (2 h of treatment) or a long-aging conventional hydrothermal process (4 days of treatment). The results confirm our previous data [35,36] indicating two different mechanisms for the zeolite synthesis represented by the direct fast zeolite precipitation using ultrasonic method and by geopolymer formation with a subsequent slower zeolite growth within the amorphous mass applying the hydrothermal process. Moreover, the data confirmed that the precipitation mechanism control of zeolite formation by sonication is also responsible for the stability of the synthetic products over time. However, a stronger antiferromagnetic contribution is observed after the longer hydrothermal processes. The transformation of geopolymers into well-organized crystals characterizing the mechanism of zeolite formation by hydrothermal process is responsible for a slow but progressive transformation of metastable EMT and FAU-type zeolite into sodalite also using obsidian as raw material. However, the data indicate that this transformation into more stable forms is as fast as the time of hydrothermal water bath time is shorter.

Author Contributions: C.B.: Conceptualization, Formal analysis, Writing original draft, Writing review & editing. D.P.: Formal analysis, Writing original draft, Writing review & editing. G.V.: Formal analysis, Writing original draft. M.A.: Formal analysis, Writing original draft, Writing review & editing. A.P.R.: Writing original draft. F.C.: Formal analysis, Writing original draft. All authors have read and agreed to the published version of the manuscript.

Funding: This research received no external funding.

Acknowledgments: The author thanks colleague Antonio Lettino for assistance with scanning electron microscopy analysis.

Conflicts of Interest: The authors declare no conflict of interest.

References

1. Belviso, C.; Cavalcante, F.; Ragone, P.; Fiore, S. Immobilization of Ni by synthesising zeolite at low temperatures in a polluted soil. *Chemosphere* **2010**, *78*, 1172–1176. [[CrossRef](#)] [[PubMed](#)]
2. Imran, A.; Bramer, E.A.; Seshan, K.; Brem, G. Catalytic Flash Pyrolysis of Biomass Using Different Types of Zeolite and Online Vapor Fractionation. *Energies* **2016**, *9*, 187. [[CrossRef](#)]
3. Belviso, C.; Cavalcante, F.; Di Gennaro, S.; Lettino, A.; Palma, A.; Ragone, P.; Fiore, S. Removal of Mn from aqueous solution using fly ash and its hydrothermal synthetic zeolite. *J. Environ. Manag.* **2014**, *137*, 16–22. [[CrossRef](#)] [[PubMed](#)]
4. Kim, H.S.; Jeong, N.C.; Yoon, K.B. Photovoltaic Effects of CdS and PbS Quantum Dots Encapsulated in Zeolite Y. *Langmuir* **2011**, *27*, 14678–14688. [[CrossRef](#)]
5. Ferreira, L.; Fonseca, A.M.; Botelho, G.; Almeida-Aguiar, C.; Neves, I. Antimicrobial activity of faujasite zeolites doped with silver. *Microporous Mesoporous Mater.* **2012**, *160*, 126–132. [[CrossRef](#)]
6. Belviso, C.; Cavalcante, F.; Ragone, P.; Fiore, S. Immobilization of Zn and Pb in Polluted Soil by In Situ Crystallization Zeolites from Fly Ash. *Water Air Soil Pollut.* **2012**, *223*, 5357–5364. [[CrossRef](#)]
7. Amorim, R.; Vilaça, N.; Martinho, O.; Reis, R.M.; Sardo, M.; Rocha, J.; Fonseca, A.M.; Baltazar, F.; Neves, I. Zeolite Structures Loading with an Anticancer Compound as Drug Delivery Systems. *J. Phys. Chem. C* **2012**, *116*, 25642–25650. [[CrossRef](#)]
8. Tsotsalas, M.M.; Kopka, K.; Luppi, G.; Wagner, S.; Law, M.P.; Schäfers, M.; De Cola, L. Encapsulating 111In in Nanocontainers for Scintigraphic Imaging: Synthesis, Characterization, and In Vivo Biodistribution. *ACS Nano* **2010**, *4*, 2486. [[CrossRef](#)]
9. Gjyli, S.; Korpa, A.; Tabanelli, T.; Trettin, R.; Cavani, F.; Belviso, C. Higher conversion rate of phenol alkylation by using synthetic fly ash-based zeolites. *Microporous Mesoporous Mater.* **2019**, *284*, 434–442. [[CrossRef](#)]
10. Barquist, K.; Larsen, S.C. Chromate adsorption on bifunctional, magnetic zeolite composites. *Microporous Mesoporous Mater.* **2010**, *130*, 197–202. [[CrossRef](#)]
11. Deng, Y.; Deng, C.; Qi, D.; Liu, C.; Liu, J.; Zhang, X.; Zhao, D. Synthesis of Core/Shell Colloidal Magnetic Zeolite Microspheres for the Immobilization of Trypsin. *Adv. Mater.* **2009**, *21*, 1377–1382. [[CrossRef](#)]
12. Yamaura, M.; Fungaro, D.A. Synthesis and characterization of magnetic adsorbent prepared by magnetite nanoparticles and zeolite from coal fly ash. *J. Mater. Sci.* **2013**, *48*, 5093–5101. [[CrossRef](#)]
13. Cao, J.; Liu, X.; Fu, R.; Tan, Z.-Y. Magnetic P zeolites: Synthesis, characterization and the behavior in potassium extraction from seawater. *Sep. Purif. Technol.* **2008**, *63*, 92–100. [[CrossRef](#)]
14. Belviso, C.; Kharchenko, A.; Agostinelli, E.; Cavalcante, F.; Peddis, D.; Varvaro, G.; Yaacoub, N.; Mintova, S. Red mud as aluminium source for the synthesis of magnetic zeolite. *Microporous Mesoporous Mater.* **2018**, *270*, 24–29. [[CrossRef](#)]
15. Belviso, C.; Agostinelli, E.; Belviso, S.; Cavalcante, F.; Pascucci, S.; Peddis, D.; Varvaro, G.; Fiore, S. Synthesis of magnetic zeolite at low temperature using a waste material mixture: Fly ash and red mud. *Microporous Mesoporous Mater.* **2015**, *202*, 208–216. [[CrossRef](#)]
16. Fabiano, B.; Reverberi, A.P.; Varbanov, P.S. Safety opportunities for the synthesis of metal nanoparticles and short-cut approach to workplace risk evaluation. *J. Clean. Prod.* **2019**, *209*, 297–308. [[CrossRef](#)]
17. Belviso, C. State-of-the-art applications of fly ash from coal and biomass: A focus on zeolite synthesis processes and issues. *Prog. Energy Combust. Sci.* **2018**, *65*, 109–135. [[CrossRef](#)]

18. Zhao, Y.; Liu, Z.; Li, W.; Zhao, Y.; Pan, H.; Liu, Y.; Li, M.; Kong, L.; He, M. Synthesis, characterization, and catalytic performance of high-silica Y zeolites with different crystallite size. *Microporous Mesoporous Mater.* **2013**, *167*, 102–108. [[CrossRef](#)]
19. Brent, R.; Stevens, S.M.; Terasaki, O.; Anderson, M.W. Coaxial Core Shell Overgrowth of Zeolite L—dependence on Original Crystal Growth Mechanism. *Cryst. Growth Des.* **2010**, *10*, 5182–5186. [[CrossRef](#)]
20. Cheng, Y.; Wang, L.; Li, J.-S.; Yang, Y.-C.; Sun, X.-Y. Preparation and characterization of nanosized ZSM-5 zeolites in the absence of organic template. *Mater. Lett.* **2005**, *59*, 3427–3430. [[CrossRef](#)]
21. Song, W.; Grassian, V.H.; Larsen, S.C. High yield method for nanocrystalline zeolite synthesis. *Chem. Commun.* **2005**, *23*, 2951–2953. [[CrossRef](#)] [[PubMed](#)]
22. Ng, E.-P.; Delmotte, L.; Mintova, S. Environmentally benign synthesis of nanosized aluminophosphate enhanced by microwave heating. *Green Chem.* **2008**, *10*, 1043–1048. [[CrossRef](#)]
23. Cundy, C.S.; Cox, P.A. The hydrothermal synthesis of zeolites: Precursors, intermediates and reaction mechanism. *Microporous Mesoporous Mater.* **2005**, *82*, 1–78. [[CrossRef](#)]
24. Gordon, J.; Kazemian, H.; Rohani, S. Rapid and efficient crystallization of MIL-53(Fe) by ultrasound and microwave irradiation. *Microporous Mesoporous Mater.* **2012**, *162*, 36–43. [[CrossRef](#)]
25. Askari, S.; Alipour, S.M.; Halladj, R.; Farahani, M.H.D.A. Effects of ultrasound on the synthesis of zeolites: A review. *J. Porous Mater.* **2012**, *20*, 285–302. [[CrossRef](#)]
26. Tompsett, G.A.; Conner, W.C.; Yngvesson, K.S. Microwave Synthesis of Nanoporous Materials. *ChemPhysChem* **2006**, *7*, 296–319. [[CrossRef](#)]
27. Li, Y.; Yang, W. Microwave synthesis of zeolite membranes: A review. *J. Membr. Sci.* **2008**, *316*, 3–17. [[CrossRef](#)]
28. Parnham, E.R.; Morris, R.E. Ionothermal Synthesis of Zeolites, Metal–Organic Frameworks, and Inorganic–Organic Hybrids. *Accounts Chem. Res.* **2007**, *40*, 1005–1013. [[CrossRef](#)]
29. Belviso, C.; Cavalcante, F.; Fiore, S. Synthesis of zeolite from Italian coal fly ash: Differences in crystallization temperature using seawater instead of distilled water. *Waste Manag.* **2010**, *30*, 839–847. [[CrossRef](#)]
30. Belviso, C.; Cavalcante, F.; Huertas, F.J.; Lettino, A.; Ragone, P.; Fiore, S. The crystallisation of zeolite (X- and A-type) from fly ash at 25 °C in artificial seawater. *Micropor. Mesopor. Mater.* **2012**, *162*, 115–121. [[CrossRef](#)]
31. Valtchev, V.P.; Tosheva, L.; Bozhilov, K.N. Synthesis of Zeolite Nanocrystals at Room Temperature. *Langmuir* **2005**, *21*, 10724–10729. [[CrossRef](#)] [[PubMed](#)]
32. Ng, E.-P.; Chateigner, D.; Bein, T.; Valtchev, V.; Mintova, S. Capturing Ultrasmall EMT Zeolite from Template-Free Systems. *Sci.* **2011**, *335*, 70–73. [[CrossRef](#)]
33. Zhu, G.; Qiu, S.; Yu, J.; Sakamoto, Y.; Xiao, F.; Xu, A.R.; Terasaki, O. Synthesis and Characterization of High-Quality Zeolite LTA and FAU Single Nanocrystals. *Chem. Mater.* **1998**, *10*, 1483–1486. [[CrossRef](#)]
34. Rakoczy, R.A.; Traa, Y. Nanocrystalline zeolite A: Synthesis, ion exchange and dealumination. *Microporous Mesoporous Mater.* **2003**, *60*, 69–78. [[CrossRef](#)]
35. Belviso, C. Ultrasonic vs hydrothermal method: Different approaches to convert fly ash into zeolite. How they affect the stability of synthetic products over time? *Ultrason. Sonochemistry* **2018**, *43*, 9–14. [[CrossRef](#)] [[PubMed](#)]
36. Belviso, C.; Lettino, A.; Cavalcante, F. Influence of Synthesis Method on LTA Time-Dependent Stability. *Molecules* **2018**, *23*, 2122. [[CrossRef](#)]
37. Ng, E.-P.; Awala, H.; Tan, K.-H.; Adam, F.; Retoux, R.; Mintova, S. EMT-type zeolite nanocrystals synthesized from rice husk. *Microporous Mesoporous Mater.* **2015**, *204*, 204–209. [[CrossRef](#)]
38. Franus, W.; Wdowin, M.; Franus, M. Synthesis and characterization of zeolites prepared from industrial fly ash. *Environ. Monit. Assess.* **2014**, *186*, 5721–5729. [[CrossRef](#)]
39. Petushkov, A.; Merilis, G.; Larsen, S.C. From nanoparticles to hierarchical structures: Controlling the morphology of zeolite beta. *Microporous Mesoporous Mater.* **2011**, *143*, 97–103. [[CrossRef](#)]
40. Belviso, S.; Cavalcante, F.; Lettino, A.; Ragone, P.; Belviso, C. Fly ash as raw material for the synthesis of zeolite-encapsulated porphyrazine and metallo porphyrazine tetrapyrrolic macrocycles. *Microporous Mesoporous Mater.* **2016**, *236*, 228–234. [[CrossRef](#)]
41. Belviso, C.; Cavalcante, F.; Lettino, A.; Fiore, S. Effects of ultrasonic treatment on zeolite synthesized from coal fly ash. *Ultrason. Sonochemistry* **2011**, *18*, 661–668. [[CrossRef](#)]
42. Lee, T.P.; Saad, B.; Ng, E.-P.; Salleh, B. Zeolite Linde Type L as micro-solid phase extraction sorbent for the high performance liquid chromatography determination of ochratoxin A in coffee and cereal. *J. Chromatogr. A* **2012**, *1237*, 46–54. [[CrossRef](#)]

43. Belviso, C.; Cavalcante, F.; Fiore, S. Ultrasonic waves induce rapid zeolite synthesis in a seawater solution. *Ultrason. Sonochemistry* **2013**, *20*, 32–36. [[CrossRef](#)] [[PubMed](#)]
44. Holler, H.; Wirsching, G.U. Zeolite formation from fly ash. *Fortschr Miner.* **1985**, *63*, 21–43.
45. Ghasemi, Z.; Younesi, H.; Kazemian, H. Synthesis of nanozeolite sodalite from rice husk ash without organic additives. *Can. J. Chem. Eng.* **2010**, *89*, 601–608. [[CrossRef](#)]
46. Yang, G.C.; Yang, T.-Y. Synthesis of zeolites from municipal incinerator fly ash. *J. Hazard. Mater.* **1998**, *62*, 75–89. [[CrossRef](#)]
47. Belviso, C.; Cavalcante, F.; Lettino, A.; Fiore, S. A and X-type zeolites synthesised from kaolinite at low temperature. *Appl. Clay Sci.* **2013**, *80*, 162–168. [[CrossRef](#)]
48. Gualtieri, A.F. Synthesis of sodium zeolites from a natural halloysite. *Phys. Chem. Miner.* **2001**, *28*, 719–728. [[CrossRef](#)]
49. Ríos, C.A.; Williams, C.D.; Fullen, M.A. Nucleation and growth history of zeolite LTA synthesized from kaolinite by two different methods. *Appl. Clay Sci.* **2009**, *42*, 446–454. [[CrossRef](#)]
50. Heller-Kallai, L.; Lapidés, I. Reactions of kaolinites and metakaolinites with NaOH—Comparison of different samples (Part 1). *Appl. Clay Sci.* **2007**, *35*, 99–107. [[CrossRef](#)]
51. Belviso, C.; Giannossa, L.C.; Huertas, F.J.; Lettino, A.; Mangone, A.; Fiore, S. Synthesis of zeolites at low temperatures in fly ash-kaolinite mixtures. *Microporous Mesoporous Mater.* **2015**, *212*, 35–47. [[CrossRef](#)]
52. Jiang, J.; Gu, X.; Feng, L.; Duanmu, C.; Jin, Y.; Hu, T.; Wu, J. Controllable synthesis of sodalite submicron crystals and microspheres from palygorskite clay using a two-step approach. *Powder Technol.* **2012**, *217*, 298–303. [[CrossRef](#)]
53. Liu, H.; Shen, T.; Li, T.; Yuan, P.; Shi, G.; Bao, X. Green synthesis of zeolites from a natural aluminosilicate mineral rectorite: Effects of thermal treatment temperature. *Appl. Clay Sci.* **2014**, *90*, 53–60. [[CrossRef](#)]
54. Belviso, C.; Cavalcante, F.; Niceforo, G.; Lettino, A. Sodalite, faujasite and A-type zeolite from 2:1 dioctahedral and 2:1:1 trioctahedral clay minerals. A singular review of synthesis methods through laboratory trials at a low incubation temperature. *Powder Technol.* **2017**, *320*, 483–497. [[CrossRef](#)]
55. Xiong, X.; Yuan, D.; Wu, Q.; Chen, F.; Meng, X.; Lv, R.; Dai, D.; Maurer, S.; McGuire, R.; Feyen, M.; et al. Efficient and rapid transformation of high silica CHA zeolite from FAU zeolite in the absence of water. *J. Mater. Chem. A* **2017**, *5*, 9076–9080. [[CrossRef](#)]
56. Wu, Q.; Wang, X.; Meng, X.; Yang, C.; Liu, Y.; Jin, Y.; Yang, Q.; Xiao, F.-S. Organotemplate-free, seed-directed, and rapid synthesis of Al-rich zeolite MTT with improved catalytic performance in isomerization of m-xylene. *Microporous Mesoporous Mater.* **2014**, *186*, 106–112. [[CrossRef](#)]
57. Xie, B.; Zhang, H.; Yang, C.; Liu, S.; Ren, L.; Zhang, L.; Meng, X.; Yilmaz, B.; Muller, U.; Xiao, F.-S. Seed-directed synthesis of zeolites with enhanced performance in the absence of organic templates. *Chem. Commun.* **2011**, *47*, 3945–3947. [[CrossRef](#)] [[PubMed](#)]
58. Goel, S.; Zones, S.I.; Iglesia, E. Synthesis of Zeolites via Interzeolite Transformations without Organic Structure-Directing Agents. *Chem. Mater.* **2015**, *27*, 2056–2066. [[CrossRef](#)]
59. Yuan, W.; Yuan, P.; Liu, N.; Deng, L.; Zhou, J.; Yu, W.; Chen, F. A hierarchically porous diatomite/silicalite-1 composite for benzene adsorption/desorption fabricated via a facile pre-modification in situ synthesis route. *Chem. Eng. J.* **2016**, *294*, 333–342. [[CrossRef](#)]
60. Chaisena, A.; Rangsiwatananon, K. Synthesis of sodium zeolites from natural and modified diatomite. *Mater. Lett.* **2005**, *59*, 1474–1479. [[CrossRef](#)]
61. Yao, G.; Lei, J.; Zhang, X.; Sun, Z.; Zheng, S. One-Step Hydrothermal Synthesis of Zeolite X Powder from Natural Low-Grade Diatomite. *Materials* **2018**, *11*, 906. [[CrossRef](#)]
62. Belviso, C. EMT-type zeolite synthesized from obsidian. *Microporous Mesoporous Mater.* **2016**, *226*, 325–330. [[CrossRef](#)]
63. Rani, N.; Shrivastava, J.P.; Bajpai, R. Obsidian: Alteration Study under Hydrothermal-Like Conditions for its Assessment as a Nuclear Waste Glass. *Procedia Earth Planet. Sci.* **2013**, *7*, 725–728. [[CrossRef](#)]
64. Mamedova, G.A. Hydrothermal synthesis of natrolite-type zeolite in the natural halloysite-obsidian system. *Glas. Phys. Chem.* **2014**, *40*, 380–383. [[CrossRef](#)]
65. Kawano, M. Experimental Study on the Formation of Zeolites from Obsidian by Interaction with NaOH and KOH Solutions at 150 and 200 °C. *Clays Clay Miner.* **1997**, *45*, 365–377. [[CrossRef](#)]
66. Ríos, C.A.; Williams, C.D.; Castellanos, O.M. Crystallization of low silica Na-A and Na-X zeolites from transformation of kaolin and obsidian by alkaline fusion. *Ing. Compet.* **2012**, *14*, 125–137.

67. Mameli, V.; Musinu, A.; Niznansky, D.; Peddis, D.; Ennas, G.; Ardu, A.; Lugliè, C.; Cannas, C. Much More Than a Glass: The Complex Magnetic and Microstructural Properties of Obsidian. *J. Phys. Chem.* **2016**, *120*, 27635–27645. [[CrossRef](#)]
68. Peddis, D.; Rinaldi, D.; Ennas, G.; Scano, A.; Agostinelli, E.; Fiorani, D. Superparamagnetic blocking and superspin-glass freezing in ultra small δ -(Fe_{0.67}Mn_{0.33})OOH particles. *Phys. Chem. Chem. Phys.* **2012**, *14*, 3162–3169. [[CrossRef](#)]
69. Liu, Q.; Navrotsky, A. Synthesis of nitrate sodalite: An in situ scanning calorimetric study. *Geochim. Cosmochim. Acta* **2007**, *71*, 2072–2078. [[CrossRef](#)]

Publisher's Note: MDPI stays neutral with regard to jurisdictional claims in published maps and institutional affiliations.



© 2020 by the authors. Licensee MDPI, Basel, Switzerland. This article is an open access article distributed under the terms and conditions of the Creative Commons Attribution (CC BY) license (<http://creativecommons.org/licenses/by/4.0/>).